University of Groningen

Finite strain discrete dislocation plasticity

Deshpande, VS; Needleman, A; Van der Giessen, E

Published in:
Journal of the Mechanics and Physics of Solids

DOI:
10.1016/j.jmps.2003.09.012

IMPORTANT NOTE: You are advised to consult the publisher's version (publisher's PDF) if you wish to cite from it. Please check the document version below.

Document Version
Publisher's PDF, also known as Version of record

Publication date:
2003

Link to publication in University of Groningen/UMCG research database

Citation for published version (APA):
Deshpande, VS., Needleman, A., & Van der Giessen, E. (2003). Finite strain discrete dislocation plasticity. *Journal of the Mechanics and Physics of Solids*, *51*(11-12), 2057-2083. https://doi.org/10.1016/j.jmps.2003.09.012

Copyright
Other than for strictly personal use, it is not permitted to download or to forward/distribute the text or part of it without the consent of the author(s) and/or copyright holder(s), unless the work is under an open content license (like Creative Commons).

The publication may also be distributed here under the terms of Article 25fa of the Dutch Copyright Act, indicated by the “Taverne” license. More information can be found on the University of Groningen website: https://www.rug.nl/library/open-access/self-archiving-pure/taverne-amendment.

Take-down policy
If you believe that this document breaches copyright please contact us providing details, and we will remove access to the work immediately and investigate your claim.

Downloaded from the University of Groningen/UMCG research database (Pure): http://www.rug.nl/research/portal. For technical reasons the number of authors shown on this cover page is limited to 10 maximum.

Download date: 04-06-2022

ELSEVIER

Journal of the Mechanics and Physics of Solids
51 (2003) 2057–2083

JOURNAL OF THE
MECHANICS AND
PHYSICS OF SOLIDS

www.elsevier.com/locate/jmps

Finite strain discrete dislocation plasticity

V.S. Deshpande[a], A. Needleman[b,*], E. Van der Giessen[c]

[a] *Department of Engineering, Cambridge University, Trumpington Street, Cambridge CB2 1PZ, UK*
[b] *Division of Engineering, Brown University, 182 Hope street, Providence, RI 02912-9104, USA*
[c] *Department of Applied Physics, University of Groningen, Nyenborgh 4, 9747 AG Groningen, The Netherlands*

Abstract

A framework for carrying out finite deformation discrete dislocation plasticity calculations is presented. The discrete dislocations are presumed to be adequately represented by the singular linear elastic fields so that the large deformations near dislocation cores are not modeled. The finite deformation effects accounted for are: (i) finite lattice rotations and (ii) shape changes due to slip. As a consequence of the nonlinearity, an iterative procedure is needed to solve boundary value problems. Elastic anisotropy together with lattice curvature is shown to lead to a polarization stress term in the rate boundary value problem. The general three-dimensional framework is specialized to plane strain. The plane strain specialization is implemented in a conventional finite element code and two numerical examples are given: plane strain tension of a single crystal strip and combined bending and tension of that strip. The capabilities and limitations of a conventional finite element framework for this class of problems are illustrated and discussed.

Keywords: Dislocation theory; Mechanical properties; Plastic deformation; Finite element modeling

1. Introduction

For a wide range of crystalline solids, room temperature plastic deformation occurs due to the collective motion of dislocations gliding on specific slip planes. The mobility of dislocations is what gives rise to plastic flow at stress levels relatively low compared to the theoretical strength. A consequence of dislocation glide is the rotation of the crystal lattice which changes the resolved shear stress on the slip systems and which, in turn, affects subsequent dislocation glide. The significance of lattice reorientation for

---

* Corresponding author. Tel.: +1-401-863-2863; fax: +1-401-863-9009.
E-mail address: needle@engin.brown.edu (A. Needleman).

doi:10.1016/j.jmps.2003.09.012

plastic flow has long been recognized, both experimentally and theoretically, at least within the context of continuum plasticity, see e.g. Asaro (1983).

Since the late 1980s, considerable activity has been directed at representing plastic flow in terms of the dynamics of large numbers of interacting dislocations, with the dislocations represented as line singularities in an elastic solid, see e.g. Devincre and Kubin (1994), Van der Giessen and Needleman (1995). This framework naturally accounts for both the stress enhancement due to organized dislocation structures and the stress relaxation arising from dislocation glide. Superposition of a complementary (or image) field, enables boundary value problems to be solved where plastic flow arises from the collective motion of discrete dislocations, Van der Giessen and Needleman (1995). This discrete dislocation plasticity framework has been restricted to infinitesimal deformations; both the effect of lattice reorientation on dislocation glide and the effect of geometry changes on the momentum balance have been neglected. The successes of infinitesimal deformation discrete dislocation plasticity, for example in application to thermal stress evolution in thin films, Nicola et al. (2003) and to fatigue crack growth, Deshpande et al. (2003), together with increasing computational capabilities provide the motivation for considering finite deformation effects.

Finite deformation effects in conjunction with dislocation plasticity have recently been considered. Acharya (2003) developed a finite deformation field theory for continuously distributed dislocations while El-Azab (2003) has developed a finite deformation statistical mechanics formalism for dislocation plasticity. Zbib et al. (2002) have presented a formulation where volume average plastic strain rates and plastic rotation rates, obtained from small deformation discrete dislocation plasticity, are used in a conventional continuum finite deformation viscoplastic constitutive description, so that the finite deformation effects are decoupled from the discrete dislocation dynamics. In contrast, our aim is to provide a fully coupled framework for carrying out finite deformation discrete dislocation plasticity analyses. However, the large deformations that occur near the dislocation line (the dislocation core region), and which are not well-represented by linear elasticity, are not modeled.

We focus attention on: (i) finite deformation-induced lattice rotations and (ii) the shape change due to slip. The effect of lattice rotations and finite geometry changes on the motion of the discrete dislocations is accounted for. The stress and deformation fields associated with individual dislocations are assumed to be accurately described, outside of the dislocation core region, by linear elasticity. The key difference from conventional continuum plasticity formulations, which average over the dislocations, is that dislocations are treated individually while they move through the elastic continuum. The displacement field in this continuum is only piecewise continuous; the slip induced by dislocation motion gives rise to a jump in the displacement field. Except for these jumps, the gradient of the displacement field describes the deformation of the crystal lattice. Furthermore, due to slip interior material points can become boundary material points.

As in conventional continuum plasticity, a crystal is characterized by the orientation of a set of lattice vectors at each material point as well as by the position of the material points. At the current time, the geometry of the solid, the orientation of the lattice vectors and the positions of all dislocations are assumed known. An increment of external loading is prescribed. The updated geometry, lattice vector orientation and dislocation positions need to be determined. As in the infinitesimal deformation case, the solution of the finite deformation rate boundary value problem is represented in terms of known, singular solutions for the discrete dislocations and a complementary (image) solution that enforces the boundary conditions. This complementary solution is non-singular. The finite geometry changes are strongly coupled with the discrete dislocation dynamics. As a consequence, an iterative procedure is required at each time step to obtain the complementary solution.

We begin by presenting the finite deformation discrete dislocation plasticity formulation. Representing the shape change in finite deformation discrete dislocation plasticity requires the development of numerical methods allowing for displacement fields that are only piecewise continuous. Although an appropriate numerical method is not currently available, this is a topic of current research, e.g. Moës et al. (1999), Daux et al. (2000), Wells et al. (2002) and Remmers et al. (2003). Awaiting such a method, an implementation within a conventional finite element framework is presented. This involves averaging the slip over an element and is inherently approximate. It does, however, permit some effects of finite lattice rotations and shape changes to be illustrated.

2. Finite strain discrete dislocation formulation

We consider a crystalline solid with plastic deformation taking place by glide of a collection of discrete dislocations, each of which is represented as an elastic singular field, along a specified set of crystallographic directions.

As in continuum crystal plasticity, a distinction is made between deformation of the lattice and deformation of the material. At each material point, a set of three orthonormal vectors, define the orientation of the lattice. Stress is related to the deformation of the lattice by an elastic constitutive relation. The basic assumptions are: (i) dislocation glide is the mechanism of plastic deformation; (ii) the elastic properties are unaffected by dislocation glide; and (iii) outside the dislocation cores, the dislocation stress, strain and displacement fields are well approximated by linear elasticity. All finite deformations arise as a consequence of the displacement jumps induced by dislocation glide. These displacement jumps lead to lattice rotations that may be finite. Hence, the finite deformation effects that the formulation aims to capture are those due to deformation-induced lattice rotations and the change in shape of the body due to slip. Additional phenomena that may be involved in finite plastic deformation, such as modified elastic properties, finite lattice strains and dislocation mobility mechanisms other than slip, are not accounted for.

Attention is confined to quasi-static deformation histories, body forces are assumed absent and an updated Lagrangian framework is used so that the current and reference configurations coincide. Cartesian tensor notation is adopted and $\dot{( )}$ denotes $\partial()/\partial t$, i.e., the material time derivative with the current configuration as reference. In the current configuration, at time t, the orientation of the lattice vectors and the dislocation configuration are assumed known. The aim is to calculate the orientation of the lattice vectors, the dislocation configuration and the change in shape of the body at time $t+\mathrm{d}t$.

2.1. Kinematics

At time t, the body contains N dislocation lines and a point along a dislocation line moves, with respect to the material, with velocity $v_i^{(I)}(x_i^{(I)})$, where $I = 1,\dots,N$ and $x_i^{(I)}$ is a point along the line of dislocation I in the current configuration. A displacement discontinuity, the slip, is associated with dislocation I. The change in position of dislocation I gives rise to a displacement rate field $\dot{\tilde{u}}_i^{(I)}(x_j,t)$ at each material point which is singular along the dislocation line. The locations of the material points comprising the line of dislocation I at time $t + \mathrm{d}t$ depend on the lattice deformation and on the slip associated with all dislocations.

The total displacement rate is written as the superposition

$$\dot{u}_i(x_j,t) = \dot{\hat{u}}_i(x_j,t) + \dot{\tilde{u}}_i(x_j,t), \tag{1}$$

where x_j denotes the position of a material point in the current (reference) configuration and

$$\dot{\tilde{u}}_i = \sum_{I=1}^{N} \dot{\tilde{u}}_i^{(I)}. \tag{2}$$

Here, $\dot{\tilde{u}}_i^{(I)}$ contains the singular terms along the line of dislocation I and $\dot{\hat{u}}_i$ is the displacement rate that arises from meeting the boundary conditions as in Van der Giessen and Needleman (1995). The displacement rate field $\dot{\tilde{u}}_i^{(I)}$ is taken to be an explicitly known displacement rate field that can be directly calculated from the glide of dislocation I, either analytically or by carrying out some separate numerical calculation, e.g. an integration along the dislocation line, which then needs to be corrected to account for the effects of glide of all dislocations and of lattice deformation.

Because of slip, the displacement rate field, $\dot{u}_i$ in Eq. (1) is not a single valued function along the dislocation lines. As a consequence, the displacement rate gradient $\dot{u}_{i,j}$ is not smooth. We use $\dot{u}^*_{i,j}$ to denote the deformation rate field with the singularity along the dislocation line removed. This field specifies the rate of deformation of the lattice. With the current configuration as reference, we write

$$\dot{\varepsilon}^*_{ij} = \frac{1}{2}[\dot{u}^*_{i,j} + \dot{u}^*_{j,i}], \quad \dot{\omega}^*_{ij} = \frac{1}{2}[\dot{u}^*_{i,j} - \dot{u}^*_{j,i}], \tag{3}$$

where $()_{,i}$ is $\partial()/\partial x_i$. The fields $\dot{\varepsilon}^*_{ij}$ and $\dot{\omega}^*_{ij}$ give the rate of stretching and spin, respectively, of lattice vectors. Excluding the singular part of $\dot{u}_{i,j}$ can be accomplished by writing

$$\dot{u}^*_{i,j}(x_k^{(I)}) = \dot{\hat{u}}_{i,j} + \sum_{J \neq I} \dot{\tilde{u}}^{(J)}_{i,j} + \dot{\Upsilon}^{(I)}_{i,j}, \tag{4}$$

where $x_k^{(I)}$ denotes a point along dislocation line I and $\dot{\Upsilon}^{(I)}_{i,j}$ are possible non-singular components of $\dot{\tilde{u}}^{(I)}_{i,j}$ (e.g., if dislocation fields for a semi-infinite solid are used). Further specification of this exclusion procedure will be given in conjunction with the numerical implementation in Section 4.

In the undeformed lattice, there is a set of crystallographic planes in which the dislocations lie and glide. The unit normal to slip plane α is denoted by $m_i^{(\alpha)}$ and $s_i^{(\alpha)}$

denotes a unit vector in slip plane α. With the current orientations of $s_i^{(\alpha)}$ and $m_i^{(\alpha)}$ denoted by $s_i^{*(\alpha)}$ and $m_i^{*(\alpha)}$, respectively, the change in orientation of lattice vectors is given by

$$\dot{s}_i^{*(\alpha)} = \dot{\omega}_{ij}^{*} s_j^{*(\alpha)}, \quad \dot{m}_i^{*(\alpha)} = \dot{\omega}_{ij}^{*} m_j^{*(\alpha)}. \tag{5}$$

In the current configuration, due to lattice curvature, $s_j^{*(\alpha)}$ and $m_j^{*(\alpha)}$ vary with position.

The position of a material point at $t + \mathrm{d}t$ is

$$x_i(t + \mathrm{d}t) = x_i(t) + \dot{u}_i \, \mathrm{d}t. \tag{6}$$

Since the displacement rate field $\dot{u}_i$ includes the slip contribution, coming, for example, from the expansion of dislocation loops, $x_i(t + \mathrm{d}t)$ is not single valued along the dislocation lines.

2.2. Continuing equilibrium

The body is in equilibrium at time t. The aim is to determine the equilibrium stress field at time $t + \mathrm{d}t$. The statement of equilibrium is

$$\sigma_{ij;j} = 0, \tag{7}$$

where σ_{ij} is the symmetric Cauchy stress. In Eq. (7), the gradient is denoted by $()_{;j}$ to emphasize that it represents $\partial()/\partial x_j(t + \mathrm{d}t)$.

It is convenient to introduce additional stress measures, the Kirchhoff stress τ_{ij} and the 2nd Piola–Kirchhoff stress S_{ij}, via

$$\tau_{ij} = J\sigma_{ij}, \tag{8}$$

and

$$\tau_{ij} = (\delta_{im} + u_{i,m})(\delta_{jn} + u_{j,n}) S_{mn}. \tag{9}$$

Here, δ_{ij} is the Kronecker delta and $J = \det(\delta_{ik} + u_{i,k})$. Since the reference and current configurations are taken to coincide, the values of the components σ_{ij}, τ_{ij} and S_{ij} coincide at time t. However, their rates do not coincide.

Analogous to the small strain formulation in Van der Giessen and Needleman (1995), the stress field is written as the superposition of the stress field due to the dislocations, in their current positions and with their current orientations, $\tilde{\sigma}_{ij}$, and an image field that enforces the boundary conditions, $\hat{\sigma}_{ij}$. Since each individual dislocation stress field is an equilibrium field (within the approximation of small elastic strains),

$$\tilde{\sigma}_{ij;j} = 0. \tag{10}$$

Hence, due to the superposition $\sigma_{ij} = \hat{\sigma}_{ij} + \tilde{\sigma}_{ij}$ we have

$$\hat{\sigma}_{ij;j} = 0. \tag{11}$$

The $(\tilde{\ })$ fields are presumed known, but the $(\hat{\ })$ fields need to be determined so that the boundary conditions are satisfied. Because of the geometric nonlinearity, in general an iterative procedure is needed to solve Eq. (11). To this end a rate problem is formulated for the $(\hat{\ })$ fields that enforce the prescribed boundary conditions. We choose to formulate this rate problem in terms of the 2nd Piola–Kirchhoff stress S_{ij}. Using the rate forms of Eqs. (8) and (9), and with the current and reference states coinciding, continuing equilibrium at time t implies

$$[\dot{S}_{ij} + S_{kj}\dot{u}_{i,k}]_{,j} = 0. \tag{12}$$

Using superposition, we write

$$\dot{S}_{ij} = \dot{\hat{S}}_{ij} + \dot{\tilde{S}}_{ij}, \tag{13}$$

where

$$\dot{\tilde{S}}_{ij} = \sum_{I=1}^{N} \dot{\tilde{S}}_{ij}^{(I)}. \tag{14}$$

Here, $\dot{\tilde{S}}_{ij}^{(I)}$ is the stress rate field associated with dislocation I. With the stress fields $\hat{\tau}_{ij}$ and $\tilde{\tau}_{ij}$ defined as

$$\hat{\tau}_{ij} = (\delta_{im} + u_{i,m})(\delta_{jn} + u_{j,n})\hat{S}_{mn} \quad \text{and} \tag{15a}$$

$$\tilde{\tau}_{ij} = (\delta_{im} + u_{i,m})(\delta_{jn} + u_{j,n})\tilde{S}_{mn}, \tag{15b}$$

respectively, the rate forms of Eqs. (10) and (11), with the current and reference configurations coinciding, imply that

$$[\dot{\tilde{S}}_{ij} + \tilde{S}_{kj}\dot{u}_{i,k}]_{,j} = 0 \quad \text{and} \tag{16a}$$

$$[\dot{\hat{S}}_{ij} + \hat{S}_{kj}\dot{u}_{i,k}]_{,j} = 0. \tag{16b}$$

One complication in the finite deformation context arises from the term $S_{kj}\dot{u}_{i,k}$ in Eq. (12), which includes the slip rate (and therefore $\dot{u}_{i,k}$ is not a smooth function). Also, since the finite deformations that occur in a small core region around the dislocation are not accounted for by the linear elastic description of dislocations, a volume surrounding the dislocation core and the slip surface is excluded in formulating the boundary value problem for $\dot{\hat{u}}_i$. We then take the limit where that volume becomes vanishingly small.

The boundary value problem for $\dot{\hat{u}}_i$ is expressed in weak form. We begin by multiplying Eq. (12) by $\delta\dot{\hat{u}}_i$ (the variation in the displacement rate field we are solving for), integrating over the volume, and then using the divergence theorem to obtain

$$\int_{\hat{V}} [\dot{S}_{ij} + S_{kj}\dot{u}_{i,k}]\delta\dot{\hat{u}}_{i,j}\,\mathrm{d}V = \int_{S} \dot{T}_i\delta\dot{\hat{u}}_i\,\mathrm{d}S - \sum_{I=1}^{N}\int_{S^{(I)}} \dot{T}_i\delta\dot{\hat{u}}_i\,\mathrm{d}S, \tag{17}$$

with $C^{(I)}$ a small volume surrounding the area swept by dislocation I in the time interval dt, $S^{(I)}$ the surface of that volume and $\hat{V} = V \setminus \sum_{I=1}^{N} C^{(I)}$, as sketched in Fig. 1a.

Standard boundary conditions are considered so that

$$\dot{u}_i = \dot{u}_i^0 \text{ on } S_u, \tag{18a}$$

$$\dot{T}_i = \dot{T}_i^0 \text{ on } S_T. \tag{18b}$$

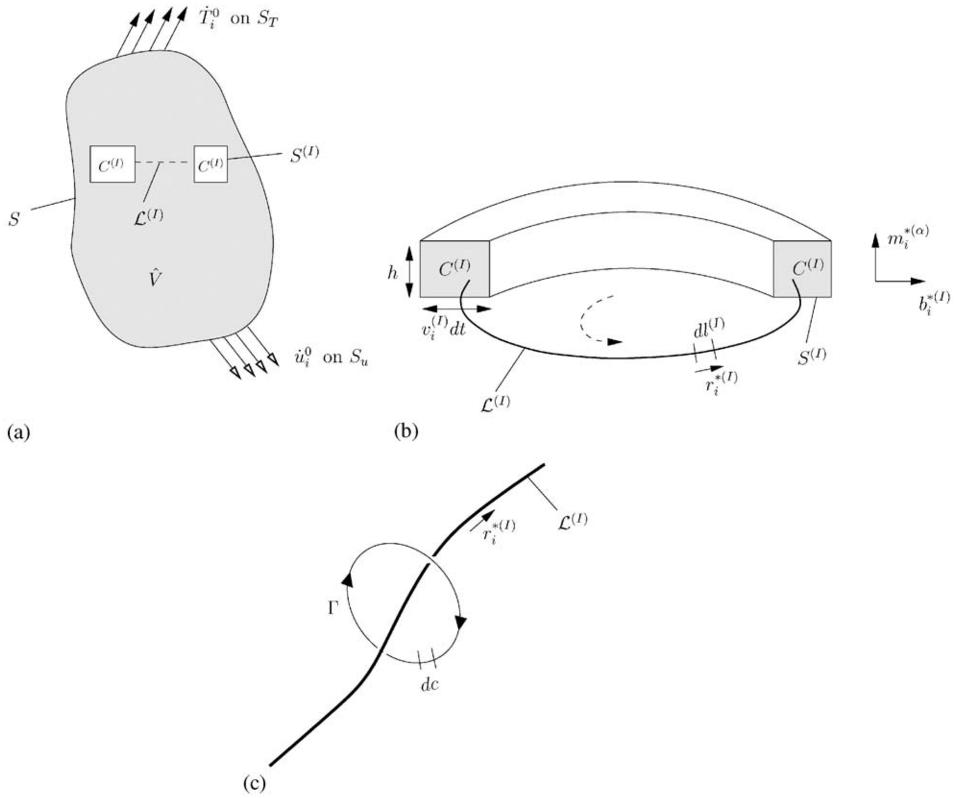

Fig. 1. (a) Body V with a volume $C^{(I)}$ around the dislocation core and slipped surface associated with dislocation loop $\mathscr{L}^{(I)}$ excluded, i.e. $V = \hat{V} \cup C^{(I)}$. (b) Open view of the excluded volume $C^{(I)}$ around dislocation loop $\mathscr{L}^{(I)}$. (c) Displacement circuit to define the local Burgers vector.

Here, $S_u \subset S$ is the part of the boundary on which displacement rates $\dot{u}_i^0$ are prescribed and S_T is the remaining part of the boundary on which traction rates $\dot{T}_i^0$ are prescribed. More complex configuration dependent boundary conditions, representing for example pressure loading, can of course also be prescribed. Due to slip interior material points can become boundary material points, and then S_u and S_T need to be appropriately modified to account for this geometry change.

The aim of the subsequent development is to derive a variational statement to serve as the basis for a numerical implementation. For this purpose note that the variational field in Eq. (17) is the continuous and differentiable field $\delta\dot{\hat{u}}_i$. Variational statements analogous to Eq. (17) can be obtained by using other trial fields; for example, the work rate identity is based on using $\delta\dot{u}_i$.

With the traction rate $\dot{\tilde{T}}_i$ on a surface with unit normal n_j due to the ($\tilde{}$) dislocation fields given by

$$\dot{\tilde{T}}_i = (\dot{\tilde{S}}_{ij} + \tilde{S}_{kj}\dot{u}_{i,k})n_j, \tag{19}$$

Eq. (16a) implies that

$$\int_{\hat{V}} [\dot{\tilde{S}}_{ij} + \tilde{S}_{kj}\dot{u}_{i,k}]\delta\dot{\hat{u}}_{i,j}\,\mathrm{d}V = \int_S \dot{\tilde{T}}_i\delta\dot{\hat{u}}_i\,\mathrm{d}S - \sum_{I=1}^{N}\int_{S^{(I)}} \dot{\tilde{T}}_i\delta\dot{\hat{u}}_i\,\mathrm{d}S. \tag{20}$$

Using superposition, Eqs. (13) and (1), along with Eq. (20), Eq. (17) takes the form

$$\int_{\hat{V}} [\dot{\hat{S}}_{ij} + \hat{S}_{kj}\dot{\hat{u}}_{i,k}]\delta\dot{\hat{u}}_{i,j}\,\mathrm{d}V = \int_{S_T} (\dot{T}_i^0 - \dot{\tilde{T}}_i)\delta\dot{\hat{u}}_i\,\mathrm{d}S$$

$$- \int_{\hat{V}} \hat{S}_{kj}\dot{\tilde{u}}_{i,k}\delta\dot{\hat{u}}_{i,j}\,\mathrm{d}V - \sum_{I=1}^{N}\int_{S^{(I)}} \dot{\hat{T}}_i\delta\dot{\hat{u}}_i\,\mathrm{d}S, \tag{21}$$

since $\delta\dot{\hat{u}}_i = 0$ on S_u.

The boundary conditions for the $(\dot{\wedge})$ fields are

$$\dot{\hat{u}}_i = \dot{u}_i^0 - \dot{\tilde{u}}_i \text{ on } S_u, \tag{22a}$$

$$\dot{\hat{T}}_i = \dot{T}_i^0 - \dot{\tilde{T}}_i \text{ on } S_T. \tag{22b}$$

where $\dot{\tilde{T}}_i$ is given by Eq. (19) and $\dot{\tilde{u}}_i$ is the discrete dislocation displacement rate on S_u including the contribution from slip.

Next, the integrals over the surfaces $S^{(I)}$ are expressed as volume integrals,

$$\sum_{I=1}^{N}\int_{S^{(I)}} \dot{\hat{T}}_i\delta\dot{\hat{u}}_i\,\mathrm{d}S = \sum_{I=1}^{N}\int_{C^{(I)}} \left[\dot{\hat{S}}_{ij} + \hat{S}_{kj}(\dot{\hat{u}}_{i,k} + \dot{\tilde{u}}_{i,k})\right]\delta\dot{\hat{u}}_{i,j}\,\mathrm{d}V, \tag{23}$$

so that Eq. (21) can be written as

$$\int_V \left[\dot{\hat{S}}_{i,j} + \hat{S}_{kj}\dot{\hat{u}}_{i,k}\right]\delta\dot{\hat{u}}_{i,j}\,\mathrm{d}V = \int_{S_T} (\dot{T}_i^0 - \dot{\tilde{T}}_i)\delta\dot{\hat{u}}_i\,\mathrm{d}S$$

$$-\sum_{I=1}^{N}\int_{(V\backslash C^{(I)})} \hat{S}_{kj}\dot{\tilde{u}}_{i,k}^{(I)}\delta\dot{\hat{u}}_{i,j}\,\mathrm{d}V$$

$$-\sum_{I=1}^{N}\int_{C^{(I)}} \hat{S}_{kj}\dot{\tilde{u}}_{i,k}^{(I)}\delta\dot{\hat{u}}_{i,j}\,\mathrm{d}V, \tag{24}$$

where we have employed the relations $V = \hat{V} \cup \sum_{I=1}^{N} C^{(I)}$ and $\dot{\tilde{u}}_{i,j} = \sum_{I=1}^{N} \dot{\tilde{u}}_{i,j}^{(I)}$.

During the time interval $\mathrm{d}t$, a dislocation line segment of length $\mathrm{d}l^{(I)}$, moving with velocity $v_i^{(I)}$ sweeps through an area of magnitude $|e_{ijk}v_i^{(I)}r_j^{*(I)}|\mathrm{d}l^{(I)}\,\mathrm{d}t$, with $r_j^{*(I)}$ a unit vector along the dislocation line segment $\mathrm{d}l^{(I)}$ and e_{ijk} the permutation tensor. The sense ascribed to $r_j^{*(I)}$ around the dislocation loop $\mathscr{L}^{(I)}$ is arbitrary and can be chosen in a right handed sense relative to $m_i^{*(\alpha)}$ as shown in Fig. 1b. The excluded volume, $C^{(I)}$, around this dislocation line segment is $h|e_{ijk}v_i^{(I)}r_j^{*(I)}m_k^{*(\alpha)}|\mathrm{d}l^{(I)}\,\mathrm{d}t$. Here, h is the distance along the normal $m_i^{*(\alpha)}$ to the slip plane on which dislocation segment $\mathrm{d}l^{(I)}$ resides (see Fig. 1b). Since consideration is restricted to dislocation glide giving rise to a displacement gradient $b^{*(I)}_i/h$ across the slip plane, in the limit $h \to 0$, in $C^{(I)}$ we set

$$\dot{\tilde{u}}^{(I)}_{i,k} = \frac{b^{*(I)}_i}{h\,\mathrm{d}t}\, m^{*(\alpha)}_k \mathrm{sign}(e_{pqr} v^{(I)}_p r^{*(I)}_q m^{*(\alpha)}_r), \tag{25}$$

where $b^{*(I)}_i$ is the Burgers vector of dislocation line segment $\mathrm{d}l^{(I)}$ in the current lattice: the local Burgers vector $b^{*(I)}_i$ of line segment $\mathrm{d}l^{(I)}$ is given by the line integral,

$$b^{*(I)}_i = \oint_{\Gamma} \frac{\partial \tilde{u}^{(I)}_i}{\partial c}\,\mathrm{d}c, \tag{26}$$

around the dislocation segment $\mathrm{d}l^{(I)}$ taken in a right-handed sense relative to $r^{*(I)}_j$, which points into the plane in Fig. 1c. Since $b^{*(I)}_i$ lies in the slip plane $b^{*(I)}_i m^{*(\alpha)}_i = 0$, and $\dot{\tilde{u}}^{(I)}_{i,i} = 0$ in $C^{(I)}$.

Using Eq. (25), the last integral on the right hand side of Eq. (24) can be expressed as

$$\int_{C^{(I)}} \hat{S}_{kj} \dot{\tilde{u}}^{(I)}_{i,k} \delta\dot{\hat{u}}_{i,j}\,\mathrm{d}V = \oint_{\mathscr{L}^{(I)}} \left[\hat{S}_{kj} b^{*(I)}_i m^{*(\alpha)}_k (e_{pqr} v^{(I)}_p r^{*(I)}_q m^{*(\alpha)}_r)\right] \delta\dot{\hat{u}}_{i,j}\,\mathrm{d}l^{(I)}, \tag{27}$$

where $\mathrm{d}V = h|e_{pqr} v^{(I)}_p r^{*(I)}_q m^{*(\alpha)}_r|\,\mathrm{d}l^{(I)}\,\mathrm{d}t$ has been used. Substituting Eq. (27) into Eq. (24) gives the weak form of the equations for the $\dot{\hat{u}}_i$ field

$$\int_V \left[\dot{\hat{S}}_{ij} + \hat{S}_{kj}\dot{\hat{u}}_{i,k}\right] \delta\dot{\hat{u}}_{i,j}\,\mathrm{d}V = \int_{S_T} (\dot{T}^0_i - \dot{\tilde{T}}_i)\delta\dot{\hat{u}}_i\,\mathrm{d}S - \sum_{I=1}^{N} \int_{(V\setminus C^{(I)})} \hat{S}_{kj}\dot{\tilde{u}}^{(I)}_{i,k}\delta\dot{\hat{u}}_{i,j}\,\mathrm{d}V$$

$$- \sum_{I=1}^{N} \oint_{\mathscr{L}^{(I)}} \left[\hat{S}_{kj} b^{*(I)}_i m^{*(\alpha)}_k (e_{pqr} v^{(I)}_p r^{*(I)}_q m^{*(\alpha)}_r)\right] \delta\dot{\hat{u}}_{i,j}\,\mathrm{d}l^{(I)}. \tag{28}$$

Since $|e_{pqr} r^{*(I)}_q m^{*(\alpha)}_r|$ is the magnitude of the pth-component of the unit normal to the dislocation line in the slip plane, $|e_{pqr} v^{(I)}_p r^{*(I)}_q m^{*(\alpha)}_r|$ is the magnitude of the glide velocity normal to the dislocation line, $V^{(I)}_{\mathrm{gln}}$. The last term on the right-hand side of Eq. (28) can then be written as

$$\sum_{I=1}^{N} \pm \oint_{\mathscr{L}^{(I)}} \hat{\mathscr{T}}_j b^{*(I)}_i V^{(I)}_{\mathrm{gln}} \delta\dot{\hat{u}}_{i,j}\,\mathrm{d}l^{(I)}, \tag{29}$$

where $\hat{\mathscr{T}}_j = \hat{S}_{kj} m^{*(\alpha)}_k$ is the traction on the glide plane. The sign in Eq. (29) depends on the sign convention for $r^{*(I)}_q$.

The constitutive relation for lattice elasticity can be written as

$$\dot{S}_{ij} = L_{ijkl}\dot{\varepsilon}^*_{kl} \quad \text{in } V, \tag{30}$$

where L_{ijkl} is the tensor of elastic moduli. Here, attention is confined to isotropic elasticity so that the moduli are unaffected by lattice rotation and remain position independent. The consequences of elastic anisotropy are discussed in Section 2.3. Using superposition, Eq. (13), $\dot{\hat{S}}_{ij}$ and $\dot{\tilde{S}}_{ij}$ are given by

$$\dot{\hat{S}}_{ij} = L_{ijkl}\dot{\hat{\varepsilon}}_{kl}, \quad \dot{\tilde{S}}_{ij} = L_{ijkl}\dot{\tilde{\varepsilon}}_{kl}, \tag{31}$$

where

$$\dot{\hat{\varepsilon}}_{kl} = \frac{1}{2}\left(\dot{\hat{u}}_{k,l} + \dot{\hat{u}}_{l,k}\right), \quad \dot{\tilde{\varepsilon}}_{kl} = \frac{1}{2}\left(\dot{\tilde{u}}_{k,l} + \dot{\tilde{u}}_{l,k}\right). \tag{32}$$

The first of Eqs. (31) and (32) are substituted into Eq. (28) to complete the specification of the weak form of the governing equations for the unknown $\dot{\hat{u}}_i$.

With the reference and current configurations coinciding, differentiation of Eq. (15a) gives the relation between the components of the material rate of Kirchhoff stress, $\dot{\hat{\tau}}_{ij}$, and $\dot{\hat{S}}_{ij}$ as

$$\dot{\hat{\tau}}_{ij} = \dot{\hat{S}}_{ij} + \dot{u}^*_{i,m}\hat{S}_{mj} + \dot{u}^*_{j,n}\hat{S}_{in} \tag{33}$$

after subtracting the singular part of $\dot{u}_{i,m}$ since $\dot{u}_{i,m} = \dot{u}^*_{i,m}$ in V. Using the first of Eqs. (31) in Eq. (33) gives

$$\dot{\hat{\tau}}_{ij} = L_{ijkl}\dot{\hat{\varepsilon}}_{kl} + \dot{u}^*_{i,m}\hat{S}_{mj} + \dot{u}^*_{j,n}\hat{S}_{in}, \tag{34}$$

with which the stress is updated by $\hat{\tau}_{ij}(t+\mathrm{d}t) = \hat{\tau}_{ij}(t) + \dot{\hat{\tau}}_{ij}\,\mathrm{d}t$. Formally, there is a relation analogous to Eq. (34) for the singular $\dot{\tilde{\tau}}_{ij}$ field. However, it is more effective to calculate $\tilde{\tau}_{ij}(t+\mathrm{d}t)$ directly from the stress fields of the individual dislocations in their positions and orientations at time $t+\mathrm{d}t$.

We note that Eq. (34) can also be interpreted as the elastic constitutive relation expressed in terms of the components of the lattice-convected Kirchhoff stress rate $\dot{\boldsymbol{\tau}}^{*c} = \dot{\hat{S}}_{ij}\mathbf{e}^*_i \otimes \mathbf{e}^*_j$, where $\mathbf{e}^*_i$ are base vectors that rotate and deform with the lattice.

At $t+\mathrm{d}t$, the components of the 2nd Piola–Kirchhoff stress, $\hat{S}_{ij}$, are set equal to $\hat{\tau}_{ij}$. Since outside the dislocation cores $J \approx 1$, so that $\hat{\sigma}_{ij} \approx \hat{\tau}_{ij}$, the weak form of Eq. (11) can be written as

$$\int_V \hat{S}_{ij}\delta\dot{\hat{u}}_{i,j}\,\mathrm{d}V = \int_{S_T} (T^0_i - \tilde{T}_i)\delta\dot{\hat{u}}_i\,\mathrm{d}S. \tag{35}$$

An iterative solution procedure is required since all terms in Eq. (28) are not known at the beginning of the time step. In particular, contributions to the $(\dot{\tilde{\ }})$ fields come from: (i) glide of dislocation I which is obtained from a constitutive rule; (ii) rotation of the lattice at the current position of dislocation I; (iii) the change in the position of dislocation I due to the glide of other dislocations; and (iv) the change in the position of dislocation I due to the complementary field $\dot{\hat{u}}_i$. In the first iteration, the contributions (ii) to (iv) are not known. In subsequent iterations, the dislocation positions are fixed with respect to the material, i.e. the glide velocities $V^{(I)}_{\mathrm{gln}}$ of all dislocations are set zero and the contribution, $\Delta\tilde{u}_i$, to $\dot{\tilde{u}}_i\,\mathrm{d}t$ from (ii) to (iv) is obtained by solving Eq. (28) repeatedly until Eq. (35) is satisfied in the configuration at time $t+\mathrm{d}t$. The iterative procedure alleviates numerical difficulties in evaluating the integral over $V \setminus C^{(I)}$ in

Eq. (28); errors made in that integration will be resolved during the iterative process based on Eq. (35). More details are given in Section 4.

2.3. Elastic anisotropy

In the finite deformation context, the boundary value problem formulation needs to account for the effect of non-uniform lattice rotations on elastic anisotropy. Due to the deformation induced change in lattice vectors, the components of the tensor of elastic moduli, L_{ijkl}, at time $t + \mathrm{d}t$ are given by

$$L_{ijkl}(t + \mathrm{d}t) = (\delta_{im} + \dot{u}^*_{i,m}\,\mathrm{d}t)(\delta_{jn} + \dot{u}^*_{j,n}\,\mathrm{d}t)(\delta_{kp} + \dot{u}^*_{k,p}\,\mathrm{d}t)(\delta_{lq} + \dot{u}^*_{l,q}\,\mathrm{d}t)L_{mnpq}(t). \tag{36}$$

For small elastic strains, the displacement gradient terms in Eq. (36) can be replaced by the corresponding lattice rotations, i.e. $\dot{u}^*_{i,m} \approx \dot{\omega}^*_{im}$. Thus, anisotropic moduli L_{ijkl} are, in general, position dependent in the current configuration, as a consequence of lattice rotation, even if the L_{ijkl} are position independent in the unstressed configuration. Furthermore, the moduli may vary along the dislocation lines.

In order to use the fields of dislocations in a homogeneous elastic solid as the $(\tilde{\ })$ fields, dislocation lines can be discretized into N dislocation segments. Denoting the tensor of elastic moduli associated with dislocation line segment $\mathrm{d}l^{(I)}$ by $L^{(I)}_{ijkl}(x^{(I)}_p)$, where $x^{(I)}_p$ is the position of the line segment $\mathrm{d}l^{(I)}$, the dislocation stress rate field $\dot{\tilde{S}}^{(I)}_{ij}$ associated with the line segment $\mathrm{d}l^{(I)}$ is given by

$$\dot{\tilde{S}}^{(I)}_{ij} = L^{(I)}_{ijkl}(x^{(I)}_p)\dot{\tilde{\varepsilon}}^{(I)}_{kl}, \qquad \dot{\tilde{\varepsilon}}^{(I)}_{kl} = \frac{1}{2}\left(\dot{\tilde{u}}^{(I)}_{k,l} + \dot{\tilde{u}}^{(I)}_{l,k}\right) \quad \text{in } V. \tag{37}$$

Here, $\dot{\tilde{u}}^{(I)}_i$ is the singular displacement rate field of dislocation line segment $\mathrm{d}l^{(I)}$ in a homogeneous elastic solid with elastic modulus $L^{(I)}_{ijkl}(x^{(I)}_p)$. The sums in Eqs. (2) and (14) are now interpreted as summations over the N dislocation line segments and Eq. (28) is modified accordingly. Furthermore, the elastic constitutive relation for $\dot{\hat{S}}_{ij}$ in Eq. (31) becomes

$$\dot{\hat{S}}_{ij} = L_{ijkl}(x_p)\dot{\hat{\varepsilon}}_{kl} + \dot{P}_{ij} \quad \text{in } V, \tag{38a}$$

where

$$\dot{P}_{ij} = \sum_{I=1}^{N} \left[L_{ijkl}(x_p) - L^{(I)}_{ijkl}(x^{(I)}_p)\right] \dot{\tilde{\varepsilon}}^{(I)}_{kl}. \tag{38b}$$

The sum in Eq. (38b) is over all the dislocation segments along all the dislocations lines. The polarization stress term, $\dot{P}_{ij}$, in Eq. (38) arises from the elastic inhomogeneity of the body in the current configuration and the fact that we employ $(\tilde{\ })$ fields for dislocations in a homogeneous elastic solid. Relation (38) is used in the modified Eq. (28) in place of the first of Eq. (31).

3. Plane strain specialization

Here, we specialize the general three-dimensional framework to a two-dimensional plane strain context. The x_1–x_2-plane is the plane of deformation and only straight edge dislocations parallel to the x_3-axis are considered. The crystallographic direction $s_i^{*(\alpha)}$ is taken as the slip direction and hence colinear with the Burgers vector of an edge dislocation on the αth slip system. The glide velocity of dislocation I then is $V_{\rm gln}^{(I)} = v_p^{(I)} s_p^{*(\alpha)}$. In plane strain, we use the convention that $r_i^{*(I)}$ is pointing out of the plane of deformation, so that the contour in Eq. (26) is taken in the counter-clockwise direction and define $r_k^{*(I)} = e_{ijk} s_i^{*(\alpha)} m_j^{*(\alpha)}$, where $m_j^{*(\alpha)}$ is the current local normal to the slip plane on which dislocation I resides.

Employing the above definitions, in plane strain, the rate equation (28) has the form

$$\int_A \left[\dot{\hat{S}}_{ij} + \hat{S}_{kj}\dot{\hat{u}}_{i,k}\right] \delta\dot{\hat{u}}_{i,j}\,{\rm d}A = \int_{S_T} (\dot{T}_i^0 - \dot{\tilde{T}}_i)\delta\dot{\hat{u}}_i\,{\rm d}S - \sum_{I=1}^{N} \int_{(A\backslash c^{(I)})} \hat{S}_{kj}\dot{\tilde{u}}_{i,k}^{(I)}\delta\dot{\hat{u}}_{i,j}\,{\rm d}A$$

$$+ \sum_{I=1}^{N} \left[\hat{S}_{kj} b_i^{*(I)} m_k^{*(\alpha)} v_p^{(I)} s_p^{*(\alpha)}\right]_{x = x_p^{(I)}} \delta\dot{\hat{u}}_{i,j}(x_p^{(I)}), \qquad (39)$$

where A is the area in the x_1–x_2-plane occupied by the body, $x_p^{(I)}$ is the location of edge dislocation I, $c^{(I)}$ is the excluded area around dislocation I and S_T is the portion of the boundary of A on which traction rates are prescribed. In plane strain, with edge dislocation lines parallel to the x_3-axis, the last integral in Eq. (28) reduces to a quantity evaluated at the dislocation position as given in Eq. (39).

Attention is restricted to elastically isotropic and homogeneous crystals with Young's modulus E and Poisson's ratio v. Constitutive rules for dislocation dynamics in three dimensions were given by Kubin et al. (1992) and subsequently employed by Van der Giessen and Needleman (1995) in plane strain analyses. We summarize the plane strain rules, highlighting the differences that arise due to the finite strain context.

One significant change is that dislocations are no longer confined to a fixed slip plane due to slip on intersecting slip systems. Hence, the basic entity is a slip system (i.e., the orientation in the lattice of the slip plane normal and the slip direction) rather than a slip plane. Furthermore, because of finite rotations, the orientation of a nucleated dislocation dipole (the two-dimensional analog of a nucleated loop) varies with the local deformation state.

The glide force work conjugate to infinitesimal variations of the position of dislocation I (i.e. the Peach–Koehler force) is given by

$$f^{(I)} = \left(\hat{S}_{ij} + \sum_{J \neq I} \tilde{S}_{ij}^{(J)} + \Sigma_{ij}^{(I)}\right) b_j^{*(I)} e_{pqi} r_p^{*(I)} s_q^{*(\alpha)}$$

$$\equiv \left(\hat{S}_{ij} + \sum_{J \neq I} \tilde{S}_{ij}^{(J)} + \Sigma_{ij}^{(I)}\right) b_j^{*(I)} m_i^{*(\alpha)}, \qquad (40)$$

where $\tilde{S}_{ij}^{(J)}$ the stress field of dislocation J and $\Sigma_{ij}^{(I)}$ are the non-singular components of $\tilde{S}_{ij}^{(I)}$, for example, if dislocation fields for a semi-infinite solid are used. In the updated Lagrangian scheme employed here, the components S_{ij} in the current configuration are equal to those of the Kirchhoff stress or Cauchy stress so that Eq. (40) could also be expressed in terms of τ_{ij} or σ_{ij}. The Peach–Koehler force enters the constitutive rules for dislocation glide, dislocation nucleation, and dislocation pinning at and releasing from obstacles.

The magnitude of the glide velocity $V_{\rm gln}^{(I)}$ along the current slip direction $s_i^{*(\alpha)}$ of dislocation I is taken to be linearly related to the Peach–Koehler force through the drag relation

$$V_{\rm gln}^{(I)} = \frac{1}{B} f^{(I)}, \tag{41}$$

where B is the drag coefficient. Here, we assume that the drag coefficient B is constant throughout the body. We also do not account for any change in the resistance to dislocation motion near a free surface associated with the energy required to create new free surface when the dislocation exits.

New dislocation pairs are generated by simulating Frank–Read sources. In two dimensions, this is mimicked by discrete point sources on a slip system α which generate a dislocation dipole with their Burgers vectors aligned with $s_i^{*(\alpha)}$. This occurs when the magnitude of the Peach–Koehler force at that source exceeds a critical value $\tau_{\rm nuc} b$ during a time period $t_{\rm nuc}$. The distance $L_{\rm nuc}$ between the dislocations is taken to be specified by

$$L_{\rm nuc} = \frac{E}{4\pi(1-\nu^2)} \frac{b}{\tau_{\rm nuc}}, \tag{42}$$

where b the magnitude of the Burgers vector in this elastically homogeneous isotropic solid. This choice of $L_{\rm nuc}$ ensures that the shear stress of one dislocation acting on the other is balanced by the slip system shear stress $\tau_{\rm nuc}$. Since lattice strains are assumed to remain small outside the dislocation cores, the magnitude b is unaffected by deformation.

Annihilation of two opposite signed dislocations on slip system α occurs when they are sufficiently close together. This is modeled by eliminating the two dislocations when they are within a material-dependent critical annihilation distance $L_{\rm e}$. Note that unlike the small strain formulation where only opposite signed dislocations on a given slip plane can annihilate each other, in the finite strain context opposite signed dislocations on a given slip system can annihilate each other. Thus, annihilation of two opposite signed dislocations on a particular slip system occurs when they are within $L_{\rm e}$ irrespective of their current slip planes.

Obstacles to dislocation motion are modeled as points associated with a slip system. Dislocations on the obstacle slip system get pinned as they try to pass through that point. Again, unlike in the small deformation case, dislocations and obstacles are associated with a slip system rather than a slip plane. Thus, dislocations on the obstacle slip system that pass within a specified distance, taken to be $L_{\rm e}$, get pinned to that obstacle. Pinned dislocations can only pass through an obstacle when their Peach–Koehler force exceeds an obstacle dependent value $\tau_{\rm obs} b$.

4. A conventional finite element implementation

Because the displacement field is only piecewise continuous as sketched in Fig. 2b, a finite element formulation allowing for discontinuous displacement fields is needed. Since such finite element procedures are not yet available for discrete dislocation plasticity, we explore the use of a conventional finite element method, based on displacement continuity. Accordingly, the geometry change is represented by a continuous field, which is obtained from averaging the slip over a finite element, and is thus inherently approximate. Nevertheless, this permits effects of lattice rotation and shape change to be explored.

The displacement rate field, $\dot{u}_i$, enters the formulation in two ways: (i) as a consequence of geometry changes, with the slip rates included, e.g. in Eq. (6), and (ii) through deformation gradients in which the slip rates do not enter, e.g. in Eq. (3), which are associated with the lattice deformation rate. In the conventional finite element formulation here, the material and lattice velocity gradients are given by

$$\dot{u}_{i,j} = \dot{\hat{u}}_{i,j} + \dot{u}^{\mathrm{d}}_{i,j}, \text{ and} \tag{43a}$$

$$\dot{u}^{*}_{i,j} = \dot{\hat{u}}_{i,j} + \dot{\tilde{u}}_{i,j}. \tag{43b}$$

The gradient $\dot{u}^{\mathrm{d}}_{i,j}$ is calculated by numerically differentiating the velocity field $\dot{\tilde{u}}_i$ with respect to x_j using the finite element shape functions in the current configuration and

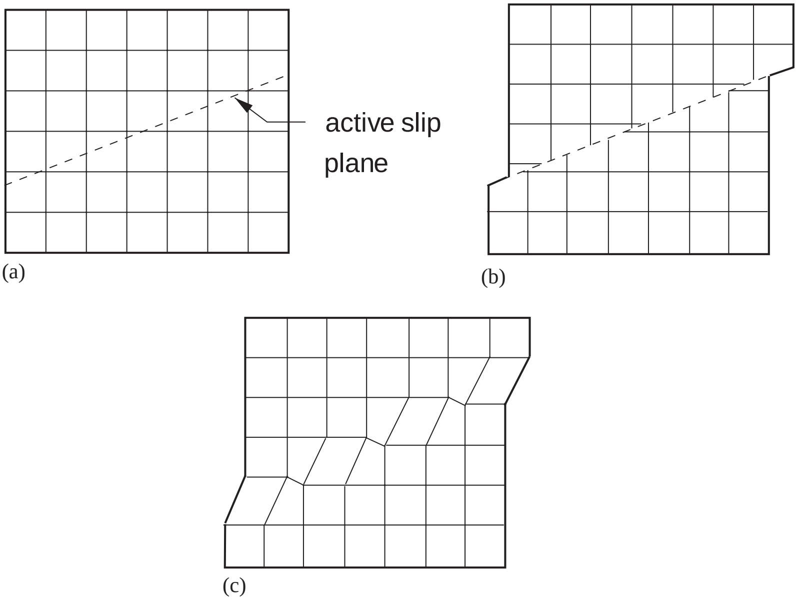

(a) (b) (c)

Fig. 2. (a) Undeformed lattice with one active slip plane. (b) Schematic showing the geometry change due to a slip discontinuity across the active slip plane. (c) Effect of smearing the slip on a finite element mesh comprised of bilinear quadrilaterals.

thereby including the slip contribution. The displacement rate field $\dot{\tilde{u}}_{i,j}$ is calculated by analytically differentiating the individual discrete dislocation displacement fields so that slip is not included.

The weak form of the rate equations governing the $\dot{\hat{u}}_i$ field is written as

$$\int_A \left[\dot{\hat{S}}_{ij} + \hat{S}_{kj}\dot{\hat{u}}_{i,k}\right] \delta\dot{\hat{u}}_{i,j}\,\mathrm{d}A = \int_{S_T} (\dot{T}_i^0 - \dot{\tilde{T}}_i)\delta\dot{\hat{u}}_i\,\mathrm{d}S - \int_A \hat{S}_{kj}\dot{u}^{\mathrm{d}}_{i,k}\delta\dot{\hat{u}}_{i,j}\,\mathrm{d}A, \tag{44}$$

where the last two integrals on the right-hand side of Eq. (28) are combined in the last integral on the right-hand side of Eq. (44) as a result of the approximation in Eq. (43a). The iterative procedure uses Eq. (44) to enforce equilibrium in the updated configuration, i.e. Eq. (35).

The effect of the approximation in Eq. (43a) is that slip is smeared out so that the change in geometry of the body due to slip is only represented approximately. This is shown schematically in Fig. 2 where the square grid represents the finite element mesh: the undeformed mesh with an active slip plane is shown in Fig. 2a, Fig. 2b depicts the deformation with a slip discontinuity across the slip plane while the approximate deformed geometry assuming bilinear elements is shown in Fig. 2c. An important consequence of the approximation is that volume constancy of the individual elements is not maintained as seen clearly in Fig. 2c. Although this volume change does not directly induce stress changes, it does limit the range of deformations that can be modeled using a conventional finite element formulation because of the approximate manner in which the geometry change is represented.

The deformation history is calculated in an incremental manner. At time t, the equilibrium fields are known and they are employed to calculate the Peach–Koehler forces on the dislocations, sources and obstacles. The rate of change of the dislocation structure caused by dislocation glide, dislocation annihilation, nucleation of new dislocations, pinning at and releasing from obstacles is determined by employing the constitutive rules.

The implementation is for plane strain using infinite medium fields for the edge dislocations, e.g. Hirth and Lothe (1968). An iterative procedure is used at each time step to satisfy Eq. (35). In the first iteration, the only contribution to the $(\dot{\tilde{\ }})$ fields is from dislocation glide and the contributions from the rotation rates of the dislocations and from the change in dislocation position due to the glide of other dislocations are not accounted for. The boundary traction and displacement rates $\dot{\tilde{T}}_i$ and $\dot{\tilde{u}}_i$, respectively, are obtained from these fields. The quantities $\dot{T}_i^0 - \dot{\tilde{T}}_i$ and $\dot{u}_i^0 - \dot{\tilde{u}}_i$ are used to set the traction and displacement boundary conditions in solving Eq. (44). With the $(\dot{\hat{\ }})$ solution thus obtained, the positions of dislocation sources and obstacles are updated using Eq. (1) while the dislocation positions are incremented by $(V_{\mathrm{gln}}^{(I)} s_i^{*(\alpha)}(t) + \dot{\hat{u}}_i + \sum_{J\neq I} \dot{\tilde{u}}_i^{(J)})\,\mathrm{d}t$. The orientations of the dislocations are tied to the lattice. Thus, the orientation of an edge dislocation on slip system α is given by $\phi^{(\alpha)} + \varphi^*$, where $\phi^{(\alpha)}$ is the orientation of slip system α in the undeformed configuration and

$$\varphi^* = \int_0^t \dot{\omega}^*_{21}\,\mathrm{d}t, \tag{45a}$$

where

$$\dot{\omega}^{*}_{21} = \frac{1}{2}\left[\dot{\hat{u}}_{2,1} + \dot{\tilde{u}}_{2,1} - \dot{\hat{u}}_{1,2} - \dot{\tilde{u}}_{1,2}\right]. \tag{45b}$$

The sign convention in Eq. (45a) is such that a counter-clockwise rotation corresponds to positive φ^{*}. In Eq. (45b), $\dot{\tilde{u}}_{i,j}$ is calculated in two steps: first, by analytically differentiating the individual discrete dislocation displacement fields with respect to x_j to remove the slip contribution and then numerically taking the difference in time $\mathrm{d}t$ to calculate the increment in $\tilde{u}_{i,j}$. This numerical difference procedure was followed so as not to build up errors associated with the numerical time integration of the singular $\dot{\tilde{u}}_{i,j}$. In the current computer code, the exclusion scheme in Eq. (4) is not implemented. Rather, the singularity in the discrete dislocation fields is eliminated by evaluating $\dot{\tilde{u}}^{(I)}_{i,j}$ from the analytical fields outside a dislocation core of radius $4b$ around dislocation I. Inside the core, the value of $\dot{\tilde{u}}^{(I)}_{i,j}$ is set equal to its value at the core boundary so that the singularity associated with $\dot{\tilde{u}}^{(I)}_{i,j}$ at the location of dislocation I is removed.

Using Eq. (34), the components of the Kirchhoff stress, $\hat{\tau}_{ij}(t + \mathrm{d}t)$, at time $t + \mathrm{d}t$ are calculated as

$$\hat{\tau}_{ij}(t + \mathrm{d}t) = \hat{\tau}_{ij}(t) + \left[L_{ijkl}\dot{\hat{\varepsilon}}_{kl} + \dot{u}^{*}_{i,m}\hat{S}_{mj}(t) + \dot{u}^{*}_{j,n}\hat{S}_{in}(t)\right]\mathrm{d}t, \tag{46}$$

where $\dot{u}^{*}_{i,m}$ is calculated in a manner similar to that used to calculate $\dot{\omega}^{*}_{21}$. The geometry is updated using Eq. (6) and, in the updated configuration, the components of the 2nd Piola–Kirchhoff stress field, $\hat{S}_{ij}$, are equal to $\hat{\tau}_{ij}$. The stress field $\tilde{S}_{ij}(t+\mathrm{d}t)$ is calculated from the analytical stress fields of the dislocations in their positions and orientations at $t + \mathrm{d}t$.

In the configuration at time $t + \mathrm{d}t$, the image field $\hat{S}_{ij}$ must satisfy Eq. (35). In general, at time $t + \mathrm{d}t$ Eq. (35) and the displacement boundary conditions will not be satisfied by solving Eq. (44) and updating the configuration. Denoting this first iteration by $k = 0$, the $(k + 1)$th iteration involves solving

$$\begin{aligned}\int_{A^{(k)}} \left[\Delta\hat{S}^{(k+1)}_{ij} + \hat{S}^{(k)}_{kj}\Delta\hat{u}^{(k+1)}_{i,k}\right]\delta\hat{u}_{i,j}\,\mathrm{d}A \\ = \int_{S^{(k)}_{T}} (T^{0}_{i} - \tilde{T}^{(k)}_{i})\delta\hat{u}_{i}\,\mathrm{d}S - \int_{A^{(k)}} \hat{S}^{(k)}_{ij}\delta\hat{u}_{i,j}\,\mathrm{d}A - \int_{A^{(k)}} \hat{S}^{(k)}_{kj}\Delta u^{\mathrm{d}(k)}_{i,k}\delta\hat{u}_{i,j}\,\mathrm{d}A,\end{aligned} \tag{47}$$

with $\Delta\hat{u}^{(k+1)}_{i} = -\Delta\tilde{u}^{(k)}_{i}$ on $S^{(k)}_{u}$. Here, $\hat{S}^{(k)}_{kj}$, $S^{(k)}_{T}$ and $S^{(k)}_{u}$ refer to quantities associated with the state after the kth iteration while $\Delta\hat{u}^{(k+1)}_{i}$ and $\Delta\hat{S}^{(k+1)}_{ij}$ are the corrections to $(\hat{\ })$ fields in the $(k + 1)$th iteration. In these iterations the dislocations do not glide ($V^{(I)}_{\mathrm{gln}}=0$) and the increments $\Delta\tilde{u}^{(k)}_{i}$ on S_u and $\Delta u^{\mathrm{d}(k)}_{i,k}$ on the right-hand side of Eq. (47) are solely the result of changes in the $(\tilde{\ })$ fields in the kth iteration: even though there is no slip contribution to $\Delta\tilde{u}^{(k)}_{i}$, for consistency $\Delta u^{\mathrm{d}(k)}_{i,k}$ in each iteration is calculated by numerically differentiating $\Delta\tilde{u}^{(k)}_{i}$ using the finite element shape functions in the configuration after the kth iteration. Also, $V^{(I)}_{\mathrm{gln}}$ is set equal to zero in calculating $\Delta\tilde{u}^{(k)}_{i}$

on S_u. For $k = 0$, the glide contributions to $\Delta u_{i,k}^{\mathrm{d}(k)}$ in Eq. (47) and to $\Delta \tilde{u}_i^{(k)}$ on S_u are explicitly subtracted out.

The positions of material points and stress $\hat{S}_{ij}$ are then updated via Eqs. (6) and (46), respectively with the $(\dot{})\,\mathrm{d}t$ terms interpreted as increments in the $(k+1)$th iteration. With no glide of the dislocations ($V_{\mathrm{gln}}^{(I)} = 0$) in these iterations, the dislocations, the dislocation sources and the dislocation obstacles are attached to material points, while the orientations of the dislocations and sources are tied to the lattice. Thus, the positions and orientations of these points are also updated. With $k \geqslant 0$, the iterations are repeated until

$$\frac{\|\Delta \hat{u}_i^{(k+1)}\|}{\left\| \sum_{m=0}^{(k+1)} \Delta \hat{u}_i^{(m)} \right\|} < \varepsilon_{\mathrm{r}}, \tag{48a}$$

and

$$\frac{\|\Delta \breve{u}_i\|}{\left\| \sum_{m=0}^{(k+1)} \Delta \hat{u}_i^{(m)} \right\|} < \varepsilon_{\mathrm{r}}, \tag{48b}$$

where ε_{r} is a specified tolerance, $\Delta \hat{u}_i^{(m)}$ is the displacement increment in the mth iteration, $\|\ \|$ denotes the Euclidean norm and $\Delta \breve{u}_i$ is the solution of

$$\int_{A^{(k)}} \left[\frac{1}{2} L_{ijkl}(\Delta \breve{u}_{k,l} + \Delta \breve{u}_{l,k}) + \hat{S}_{kj}^{(k)} \Delta \breve{u}_{i,k} \right] \delta \hat{u}_{i,j}\, \mathrm{d}A = \int_{S_T^{(k)}} (T_i^0 - \tilde{T}_i^{(k)}) \delta \hat{u}_i\, \mathrm{d}S - \int_{A^{(k)}} \hat{S}_{ij}^{(k)} \delta \hat{u}_{i,j}\, \mathrm{d}A \tag{49}$$

with $\Delta \breve{u}_i = 0$ on $S_u^{(k)}$.

In the current calculations, ε_{r} was taken as 0.01. Relation (48b) implies that equilibrium, Eq. (35), is satisfied to within a specified tolerance. In addition, at several stages of loading, Eq. (35) was checked directly.

Special treatment is needed for dislocations that exit the material through a free surface as they leave behind a step but no elastic stress or deformation field. When dislocation I exits from a free surface, dislocation I is removed from the sums in Eqs. (2) and (14). This requires subtracting out the elastic deformation field $\tilde{u}_{i,j}^{(I)}$ of dislocation I but retaining the slip displacement of dislocation I. Numerically, this is achieved by moving the dislocation along its current slip direction far away from the region being analyzed and then updating the nodal positions and the lattice orientations by the increments that result from this virtual glide of dislocation I. In addition, the image field, $\hat{S}_{ij}$, also needs to be corrected as the stress field of dislocation I is removed from the sum in Eq. (14): this correction is affected directly by the iteration procedure. Similarly when two opposite signed dislocations annihilate each other, these dislocations are removed from the sums in Eqs. (2) and (14). However, no further updating is needed in this case as the elastic fields of these two opposite-signed dislocations cancel each other.

5. Numerical examples

The finite deformation conventional finite element implementation is illustrated by considering two plane strain boundary value problems—tension and combined tension and bending. In both problems, we analyze an elastically isotropic crystal with Young's modulus $E = 70$ GPa and Poisson's ratio $\nu = 0.33$, which are representative values for aluminum. All dislocations have the same Burgers vector, $b = 0.25$ nm (which does not change during deformation since the elastic stretch of the lattice is assumed to be negligible). The undeformed crystal is of dimensions $2H \times 2W$, with $H = 4$ μm and $W = 1$ μm, and has two slip systems making angles $\phi^{(1)} = 30°$ and $\phi^{(2)} = -30°$ with the positive x_1-axis as sketched in Fig. 3. In the undeformed configuration the origin of the coordinate system is placed so that the specimen occupies a region $0 \leqslant x_1 \leqslant 2H$ and $-W \leqslant x_2 \leqslant W$, and the potentially active slip planes are equally spaced at $100b$. The slip planes are distributed such that none intersects the edges where displacements are prescribed in order to avoid numerical complications that would occur if dislocations were to attempt to exit the material through these edges.

Initially, the two slip systems are free of mobile dislocations, but dislocations can be generated from 240 discrete sources that are equally dispersed over the slip planes. The sources nucleate a dipole when the Peach–Koehler force exceeds a critical value of $\tau_{\mathrm{nuc}} b$ during a period of time $t_{\mathrm{nuc}} = 10$ ns; τ_{nuc} for the sources is taken to have a Gaussian distribution with a mean source strength $\bar{\tau}_{\mathrm{nuc}} = 50$ MPa and a standard deviation of 1 MPa. There is also a random distribution of 120 point obstacles. The obstacles pin dislocations as long as the Peach–Koehler force is below the obstacle strength $b\tau_{\mathrm{obs}}$, where $\tau_{\mathrm{obs}} = 150$ MPa. The drag coefficient for glide is $B = 10^{-4}$ Pa s, a representative value for several fcc crystals, Kubin et al. (1992), and the critical distance for annihilation is $L_{\mathrm{e}} = 6b$.

The finite deformation results are compared with results from small deformation calculations on identical crystals subject to the same boundary conditions, carried out as described in Cleveringa et al. (1999).

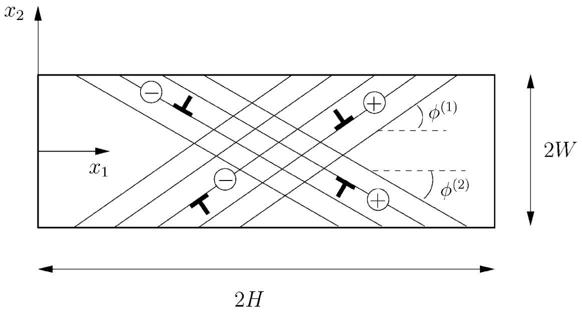

Fig. 3. Sketch of the single crystal analyzed showing the slip systems and the coordinate system. The sign convention employed for the edge dislocations is also indicated.

5.1. Tension of a single crystal

The tensile axis is aligned with the x_1-direction, see Fig. 3, and tension is imposed by prescribing

$$\dot{u}_1 = \dot{U}, \quad \dot{T}_2 = 0 \quad \text{on } x_1 = 2H + U, \tag{50a}$$

and

$$\dot{u}_1 = -\dot{U}, \quad \dot{T}_2 = 0 \quad \text{on } x_1 = -U, \tag{50b}$$

where $U = \int \dot{U}\,\mathrm{d}t$. The lateral edges, those initially on $x_2 = \pm W$, are traction free, i.e.

$$\dot{T}_1 = \dot{T}_2 = 0. \tag{51}$$

Also, $\dot{u}_2 = 0$ is imposed on two material points located at $(x_\varepsilon, 0)$ and $(2H - x_\varepsilon, 0)$ in the undeformed configuration, where $x_\varepsilon = 0.1$ μm. This simulates the constraint imposed by the grips which prevents the rotation of the specimen with respect to the loading axis in a tensile test. In addition to the boundary conditions Eqs. (50) and (51), we specify that dislocation exit from the lateral edges is unrestrained.

Since a conventional finite element method is used, interior material points do *not* become boundary points (see Fig. 2c). Thus, the traction free boundary conditions on the lateral edges are prescribed on the same material points throughout the deformation history. In a formulation allowing for slip, where internal points may become surface points, the material points on which the traction free condition need to be imposed can vary over the course of the deformation history.

A time step of $\Delta t = 0.5$ ns is needed to resolve the dislocation dynamics so a rather high loading rate $\dot{U}/H = 2000/\mathrm{s}$ is used to obtain a strain of 0.01 in 10,000 time steps. A uniform finite element grid was employed in the numerical calculations and comprised of 80×35 quadrilaterals, each built up of four triangular elements with linear displacement fields: this slightly rectangular shape of the quadrilaterals was chosen so that the orientation of the element diagonals would be near the most favorable angle for the shear bands in order to minimize the errors depicted in Fig. 2c.

We consider uniaxial tension of a single crystal oriented for symmetric double slip. The nominal stress, σ_{nom}, versus strain, U/H, response of this single crystal using the finite strain discrete dislocation plasticity with the conventional (continuous displacement) finite element method is shown in Fig. 4a. The stress, σ_{nom}, is computed as

$$\sigma_{\mathrm{nom}}(t) = -\frac{1}{2W} \int_{S_{\mathrm{L}}} T_1 \,\mathrm{d}s, \tag{52}$$

where the integration is performed along the boundary S_{L} where $x_1 = -U$.

The first dislocation activity occurs when $\sigma_{\mathrm{nom}} \approx 105$ MPa and at $\sigma_{\mathrm{nom}} \approx 115$ MPa there is a sharp drop in the load. Subsequently, the overall behavior is essentially ideally plastic up to $U/H \approx 0.04$ with the fluctuations a result of the relatively small volume over which the discrete dislocation activity is averaged. The corresponding dislocation density (number of dislocations per unit area in a central 3 μm×2 μm region) is shown in Fig. 4b: the dislocation density rises approximately linearly with strain up to the strain levels computed. For comparison purposes, the small strain discrete dislocation plasticity prediction of the tensile stress versus strain response of an identical crystal is

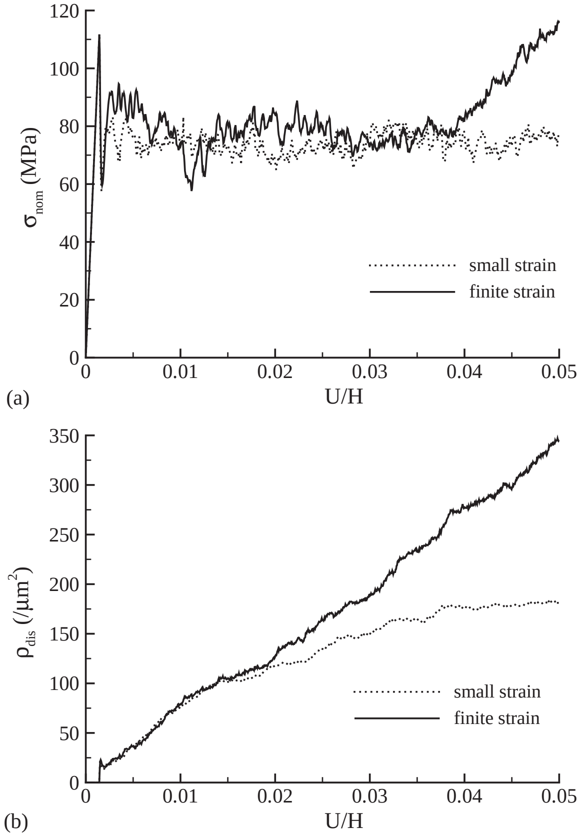

Fig. 4. Plane strain tension with $\phi^{(1)} = 30°$ and $\phi^{(2)} = -30°$. (a) Nominal tensile stress versus nominal tensile strain U/H. (b) Evolution of the total dislocation density with U/H.

also shown in Fig. 4. The small and finite strain predictions of the stress versus strain response are very similar up to a strain $U/H \approx 0.04$. However, the small strain analysis does not predict any hardening at the larger strains with the dislocation density ρ_{dis} remaining approximately constant at 175/μm^2 for $U/H > 0.03$.

The dislocation structures predicted by the finite and small strain analyses at $U/H \approx 0.05$ are shown in Figs. 5a and c, respectively. The $+$ symbols denote dislocations with Burgers vector $+b$ and the $-$ symbols denote dislocations with Burgers vector $-b$ as shown schematically in Fig. 3. A dislocation symbol is black if it corresponds to a dislocation on the slip system with $\phi^{(1)} = 30°$ and it is white if it corresponds to a dislocation on the slip system with $\phi^{(2)} = -30°$. Contours of the lattice rotation φ^* at $U/H \approx 0.05$ are also plotted in Figs. 5a and c. Fig. 5b shows the distribution of the maximum principal logarithmic strain $\ln(\lambda_{max})$, where λ_{max} is the maximum principal extension, obtained from the finite strain calculation. The finite strain calculation predicts lattice rotations of approximately $+1.5°$ and $-1°$, above and below the

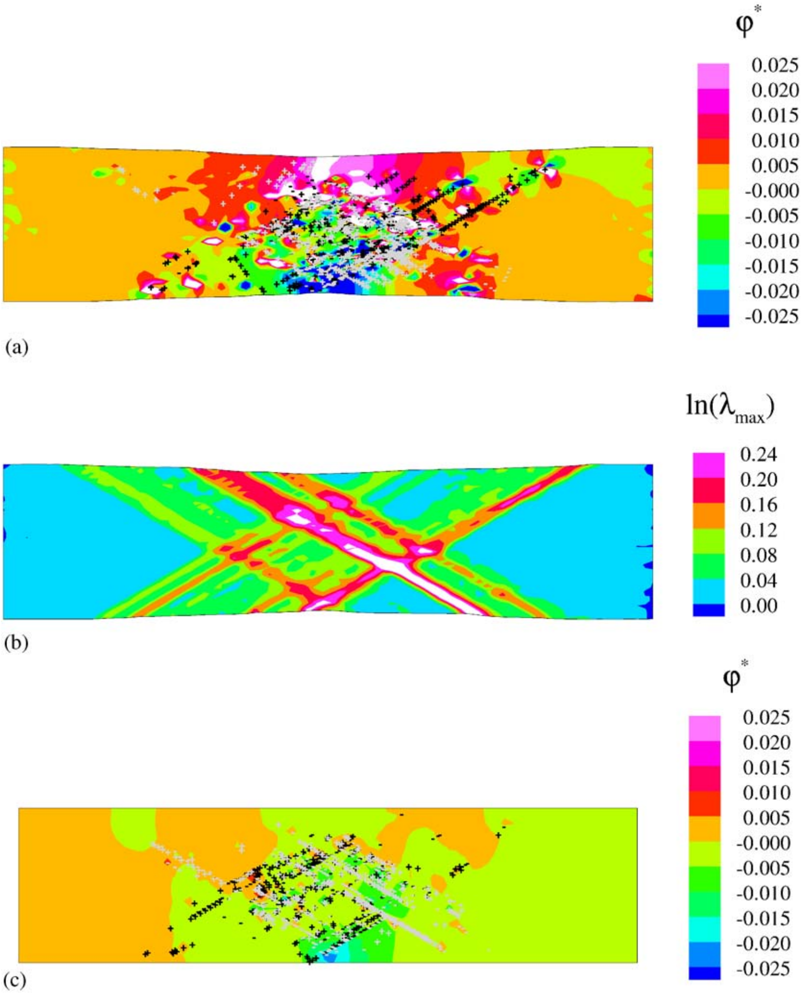

Fig. 5. Contours at $U/H \approx 0.05$ for a crystal subject to plane strain tension with $\phi^{(1)}=30^\circ$ and $\phi^{(2)}=-30^\circ$. (a) Lattice rotation φ^* and the dislocation structure as predicted by a finite strain analysis. (b) Logarithm of the maximum principal extension $\lambda_{\max}$ as predicted by a finite strain analysis. (c) Lattice rotation φ^* and the dislocation structure as predicted by a small strain analysis.

central axis of the specimen while the small strain calculation shows negligible lattice rotations at this strain level. Thus, the lattice rotations that emerge in the finite strain calculations are a result of accounting for geometry changes. Necking of the crystal at $U/H \approx 0.05$ is seen in Figs. 5a and b. For strains larger than $U/H \approx 0.04$, the finite deformation analysis exhibits a linear hardening response, with a very high hardening rate of $\mathrm{d}\sigma/\mathrm{d}(U/H) \approx G/10$, where G is the elastic shear modulus of the crystal. There are several factors that contribute to this high hardening rate including the increasing dislocation density and the lattice rotations in the necking region tending to rotate the crystal into a harder orientation. One significant contribution may come from the small, 8 μm × 2 μm, crystal size in which stress concentrations left by exiting dislocations inhibit easy glide of dislocations on the dominant slip band in Fig. 5b.

Numerical results for the finite strain tension calculation are limited to $U/H \approx 0.05$ because of the computer time required for the calculation. At $U/H \approx 0.05$, the distortion of the finite element mesh, due to the smearing out of slip depicted in Fig. 2c, is not acute and the calculations could have been continued further. However, it is expected that at some higher strain level elements along a shear band will be sufficiently distorted so as to significantly affect the accuracy of the calculations.

5.2. Combined bending and tension of a single crystal

Combined bending and tension of a crystal identical to the one analyzed in Section 5.1 is considered. The axis of bending is aligned with the x_1-direction in the undeformed state and the loading is imposed via

$$\dot{u}_1 = -\dot{\theta} x_2^0, \quad \dot{T}_2 = 0 \quad \text{on } x_1 \in S_R = \{x_1^0 = 2H\}, \tag{53a}$$

and

$$\dot{u}_1 = \dot{\theta} x_2^0, \quad \dot{T}_2 = 0 \quad \text{on } x_1 \in S_L = \{x_1^0 = 0\}. \tag{53b}$$

Here, x_i^0 are the coordinates of material points in the undeformed configuration and $\dot{\theta}$ the imposed rotation rate. Also, the lateral sides remain traction free via Eq. (51) and $\dot{u}_2 = 0$ at $(x_\varepsilon, 0)$ and $(2H - x_\varepsilon, 0)$, with $x_\varepsilon = 0.1$ μm, to prevent rigid body motion of the specimen in the x_2 direction. As in Section 5.1, dislocation exit from the lateral edges is unrestrained.

The imposed boundary conditions give rise to combined tension and bending. The bending moment is calculated as

$$M(t) = \int_{S_\mathrm{L}} T_1 x_2 \, \mathrm{d}s, \tag{54}$$

while the axial stress is defined as

$$\sigma_\mathrm{ax}(t) = -\frac{\cos\theta}{2W} \int_{S_\mathrm{L}} T_1 \, \mathrm{d}s. \tag{55}$$

The cos θ term ensures that the axial stress σ_ax is normal to the rotating ends of the specimen.

For presentation of the results, the moment M is normalized by a reference moment, M_ref, defined by

$$M_\mathrm{ref} = \frac{1}{W} \int_{-W}^{W} \sigma_\mathrm{Y} x_2^2 \, \mathrm{d}x_2 = \frac{2}{3} \sigma_\mathrm{Y} W^2, \tag{56}$$

where $\sigma_\mathrm{Y} = 115$ MPa is the peak stress in uniaxial tension, from Fig. 4a. This reference moment is the moment that would result from a linear stress distribution $\sigma_\mathrm{Y} x_2/W$ at the onset of yield.

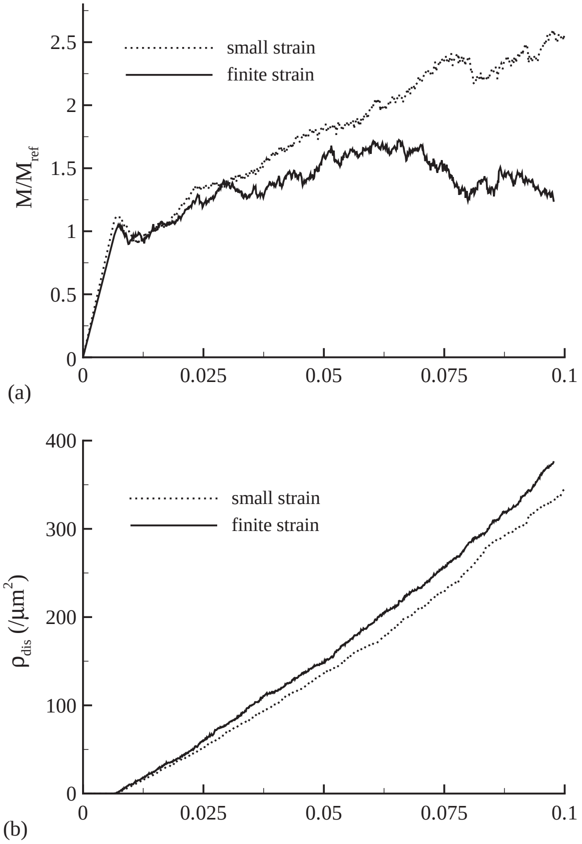

Fig. 6. Combined bending and tension with $\phi^{(1)} = 30^\circ$ and $\phi^{(2)} = -30^\circ$. (a) Normalized bending moment versus imposed rotation θ. (b) Evolution of total dislocation density with θ.

The curves of normalized moment, $M/M_{\rm ref}$, and dislocation density versus imposed rotation are shown in Figs. 6a and b, respectively, for the small and finite strain analyses with $\dot{\theta} = 4000/{\rm s}$. Consistent with the uniaxial tension results, the first dislocation activity occurs when $M/M_{\rm ref} \approx 1$ in both the small and finite strain calculations. However, unlike in the uniaxial tension case where the material exhibits ideally plastic behavior, the crystal exhibits a hardening response in bending with the bending moment increasing with rotation due to the accumulation of geometrically necessary dislocations which induce large back stresses; see Cleveringa et al. (1999) for a detailed discussion on these effects. The finite and small strain analyses predict very similar moment versus rotation responses and dislocation densities up to $\theta \approx 0.05$ ($\approx 3^\circ$): beyond this level of rotation the geometry changes become significant and the finite strain analysis predicts no continued hardening. In contrast to the tension calculation, in this bending calculation, finite strain effects give rise to a softer response than obtained from a small strain analysis. The difference between the predictions of the small strain and finite

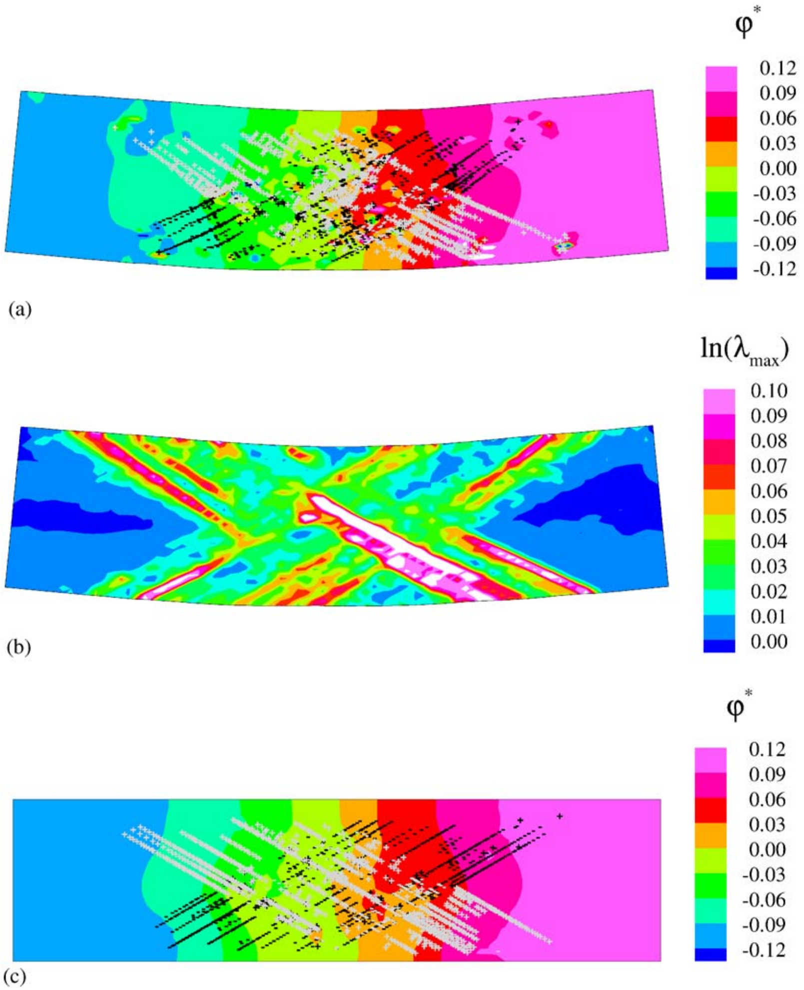

Fig. 7. Contours at $\theta \approx 0.1$ for a crystal subject to combined bending and tension with $\phi^{(1)} = 30°$ and $\phi^{(2)} = -30°$. (a) Lattice rotation φ^* and the dislocation structure as predicted by a finite strain analysis. (b) Logarithm of the maximum principal extension $\lambda_{\max}$ as predicted by a finite strain analysis. (c) Lattice rotation φ^* and the dislocation structure as predicted by a small strain analysis.

strain analyses arises, at least in part, from the difference in boundary conditions; in the small strain analysis the rotational displacements are imposed in the undeformed configuration, while in the finite strain analysis they are imposed in the current, rotated configuration.

The dislocation structure and contours of lattice rotation φ^* at an imposed rotation $\theta \approx 0.1\,(\approx 6°)$ are shown in Figs. 7a and c for the finite and small strain calculations, respectively. While both the analyses predict similar levels of lattice rotation, the curving of the slip systems due to lattice rotations occurs only in the finite strain analysis.

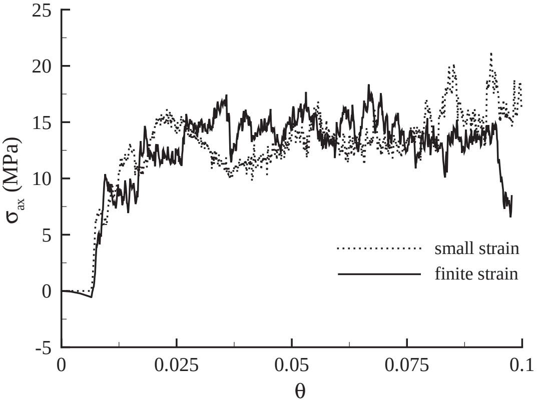

Fig. 8. The axial stress, σ_{ax}, versus imposed rotation θ for combined bending and tension as predicted by the finite strain and small strain analyses.

Fig. 7b shows contours of maximum principal logarithmic strain, $\ln(\lambda_{\mathrm{max}})$. A dominant deformation band is emerging.

The axial stress σ_{ax} as a function of the imposed rotation is shown in Fig. 8 for both the small and the finite strain analyses. Similar levels of tensile axial stress are obtained until $\theta \approx 0.09$ where there is a significant drop in the magnitude of the axial stress in the finite deformation calculation.

6. Concluding remarks

A framework has been presented for analyzing finite deformation plasticity problems where plastic flow arises from the collective motion of discrete dislocations. The main assumptions are: (i) lattice strains remain small away from dislocation cores and (ii) the elastic properties are unaffected by slip. The formulation then accounts for: (i) finite deformation-induced lattice rotations and (ii) the shape change due to slip.

The analysis reveals a strong coupling between the lattice rotations and finite geometry changes and the discrete dislocation dynamics. Even in the absence of cross slip, dislocations can change slip planes because of slip on intersecting slip systems. In addition, the orientation of a dislocation loop varies with the local deformation state. If the crystal is elastically anisotropic, this variation in orientation gives rise to position dependent moduli which results in a polarization stress term in the boundary value problem for the complementary (image) fields.

Because of slip,

$$\oint_{\Gamma} u_{i,j}\,\mathrm{d}x_j \neq 0 \tag{57}$$

for any closed path Γ that encompasses slip in the current configuration. The displacement field is only piecewise continuous. Implications of the failure to satisfy the compatibility condition (57) in the infinitesimal deformation context have been discussed by Eshelby (1956). By way of contrast, in phenomenological continuum plasticity, either local or nonlocal, an underlying assumption is that the total deformation gradient **F** can be derived from a single valued, continuous displacement field. Phenomenological nonlocal plasticity theories, such as those of Acharya and Bassani (2000), Huang et al. (2000), Fleck and Hutchinson (2001), Gurtin (2002), based on this assumption, are aimed at representing plastic flow phenomena of crystalline solids over size scales of the order of microns. The circumstances under which the assumption of a continuous displacement field is appropriate for crystal plasticity at micron size scales remain to be delineated. In this regard it is worth noting that a mathematical framework for characterizing plastic deformation with non-smooth geometry changes has been developed by Deseri and Owen (2002).

In addition to theoretical implications, the lack of continuity for the displacement rate field has a significant effect on the suitability of numerical solution methods for finite deformation discrete dislocation plasticity. We have implemented the finite deformation formulation in a conventional plane strain finite element program. The solution of two simple boundary value problems was aimed at illustrating finite deformation effects on discrete dislocation predictions. Accounting for lattice rotations and finite geometry changes increased the computational effort at each time step so that the computing time for a finite deformation analysis exceeded that for an infinitesimal deformation analysis by about a factor of 5–10 (however, no attempt has yet been made to optimize the finite deformation computational procedure). In any case, ultimately, computations using a conventional finite element method are limited by the numerics requiring a continuous displacement field. Fortunately, finite element formulations are being developed that allow arbitrary displacement discontinuities within a finite element, e.g. Moës et al. (1999), Daux et al. (2000), Wells et al. (2002), Remmers et al. (2003). Although devised for crack growth problems, this methodology seems very promising for representing the shape changes that occur in finite deformation discrete dislocation plasticity.

Acknowledgements

Support from the Materials Research Science and Engineering Center on *On Micro-and-Nano-Mechanics of Electronic and Structural Materials* at Brown University (NSF Grant DMR-0079964) is gratefully acknowledged. VSD acknowledges support from the Engineering and Physical Sciences Research Council, UK (EPSRC grant no. GR/S08107/01). We are indebted to Professors M.E. Gurtin of Carnegie-Mellon University and M. Ristinmaa of Lund University for comments which helped us improve the presentation of the formulation.

References

Acharya, A., 2003. Constitutive analysis of finite deformation field dislocation mechanics. J. Mech. Phys. Solids, to appear.

Acharya, A., Bassani, J.L., 2000. Incompatibility and crystal plasticity. J. Mech. Phys. Solids 48, 1565–1595.

Asaro, R.J., 1983. Micromechanics of crystals and polycrystals. Adv. Appl. Mech. 23, 1–115.

Cleveringa, H.H.M., Van der Giessen, E., Needleman, A., 1999. A discrete dislocation analysis of bending. Int. J. Plast. 15, 837–868.

Daux, C., Moës, N., Dolbow, J., Sukumar, N., Belytschko, T., 2000. Arbitrary branched and intersecting cracks with the extended finite element method. Int. J. Numer. Methods Eng. 48, 1741–1760.

Deseri, L., Owen, D.R., 2002. Invertible structured deformations and the geometry of multiple slip in single crystals. Int. J. Plast. 18, 833–849.

Deshpande, V.S., Needleman, A., Van der Giessen, E., 2003. Discrete dislocation plasticity modeling of short cracks in single crystals. Acta Mater. 51, 1–15.

Devincre, B., Kubin, L.P., 1994. Simulations of forest interactions and strain-hardening in fcc crystals. Model. Simul. Mater. Sci. Eng. 2, 559–570.

El-Azab, A., 2003. Statistical dislocation dynamics formalism of mesoscale crystal plasticity, to be published.

Eshelby, J.D., 1956. The continuum theory of lattice defects. In: Seitz, F., Turnbull, D. (Eds.), Solid State Physics, Vol. 3. Wiley, New York, pp. 79–144.

Fleck, N.A., Hutchinson, J.W., 2001. A reformulation of strain gradient plasticity. J. Mech. Phys. Solids 49, 2245–2271.

Gurtin, M.E., 2002. A gradient theory of single-crystal viscoplasticity that accounts for geometrically necessary dislocations. J. Mech. Phys. Solids 50, 5–32.

Hirth, J.P., Lothe, J., 1968. Theory of Dislocations. McGraw-Hill, New York.

Huang, Y., Gao, H., Nix, W.D., Hutchinson, J.W., 2000. Mechanism-based strain gradient plasticity—II. Analysis, J. Mech. Phys. Solids 48, 99–128.

Kubin, L.P., Canova, G., Condat, M., Devincre, B., Pontikis, V., Bréchet, Y., 1992. Dislocation microstructures and plastic flow: a 3D simulation. Solid State Phenomena 23-24, 455–472.

Moës, N., Dolbow, J., Belytschko, T., 1999. A finite element method for crack growth without remeshing. Int. J. Numer. Methods Eng. 46, 131–150.

Nicola, L., Van der Giessen, E., Needleman, A., 2003. Discrete dislocation analysis of size effects in thin films. J. Appl. Phys. 93, 5920–5928.

Remmers, J.J.C., de Borst, R., Needleman, A., 2003. A cohesive segments method for the simulation of crack growth. Comput. Mech. 31, 69–77.

Van der Giessen, E., Needleman, A., 1995. Discrete dislocation plasticity: a simple planar model. Model. Simul. Mater. Sci. Eng. 3, 689–735.

Wells, G.N., de Borst, R., Sluys, L.J., 2002. A consistent geometrically non-linear approach for delamination. Int. J. Numer. Meth. Eng. 54, 1333–1355.

Zbib, H.M., de la Rubia, T.D., Bulatov, V., 2002. A multiscale model of plasticity based on discrete dislocation dynamics. J. Eng. Mater. Tech. 124, 78–87.